processes

MDPI

Article

Effects of Diameter and Aspect Ratios on Particle Separation Efficiency in Hydrocyclones

Seunggi Choi [1], Wontak Choi [1], Dongmin Shin [2], Seongyool Ahn [3,*] and Yonmo Sung [2,*]

[1] Graduate Program, Department of Energy and Mechanical Engineering, Gyeongsang National University, Tongyeong-si 53064, Republic of Korea; csgcsg1248@gnu.ac.kr (S.C.); cwt005@gnu.ac.kr (W.C.)
[2] Department of Smart Energy and Mechanical Engineering, Gyeongsang National University, Tongyeong-si 53064, Republic of Korea; dmshin@gnu.ac.kr
[3] Energy and Environment R&D Center, Institute for Advanced Engineering, Yongin-si 17180, Republic of Korea
* Correspondence: syahn@iae.re.kr (S.A.); ysung@gnu.ac.kr (Y.S.)

Abstract

Hydrocyclones are widely used for solid–liquid separation, but their performance is highly sensitive to the geometric design. Previous studies often focused on individual structural parameters; however, the combined effects of the vortex finder diameter and aspect ratios on the internal flow field and particle separation behavior remain insufficiently clarified. This study conducted three-dimensional numerical simulations using the realizable k-ε turbulence model, combined with the discrete phase model. The particle size distribution behaves according to the Rosin–Rammler function. Seven different geometries were evaluated under identical operating conditions to systematically investigate how the diameter and aspect ratios influence the internal vortex structures and separation behavior. A decrease in the diameter ratio enhances the dominance of the outward centrifugal forces, which increases the downward discharge of coarse particles but also results in greater liquid entrainment through the underflow. Conversely, larger diameter ratios strengthen the secondary vortex and promote upward flow. However, this also leads to decreased recovery of fine particles due to weakened centrifugal action. Adjusting the aspect ratio effectively mitigates these tradeoffs. Increasing the cone length enhances the residence time, stabilizes the upward vortex, and improves the separation of fine particles. Although the overall separation performance shows diminishing returns beyond a certain aspect-ratio threshold, the recovery of fine particles continues to improve. The results reveal that a balance between centrifugal and drag forces is essential, which is achieved through coordinated control of the vortex finder diameter and cone geometry. This balance is critical for maintaining stable flow fields and high efficiency in fine-particle removal. The findings provide practical design guidance for hydrocyclones, particularly in applications that require enhanced recovery of fine particles and stable multiphase flow behavior.

Keywords: hydrocyclone; diameter ratio; aspect ratio; computational fluid dynamics; separation performance

check for updates

Academic Editor: Kejun Dong

Received: 27 October 2025
Revised: 23 November 2025
Accepted: 7 December 2025
Published: 9 December 2025

Citation: Choi, S.; Choi, W.; Shin, D.; Ahn, S.; Sung, Y. Effects of Diameter and Aspect Ratios on Particle Separation Efficiency in Hydrocyclones. *Processes* **2025**, *13*, 3980. https://doi.org/10.3390/pr13123980

Copyright: © 2025 by the authors. Licensee MDPI, Basel, Switzerland. This article is an open access article distributed under the terms and conditions of the Creative Commons Attribution (CC BY) license (https://creativecommons.org/licenses/by/4.0/).

1. Introduction

Hydrocyclones serve as essential equipment for separating solid particles from fluids in a wide range of industrial operations, such as mineral beneficiation, petroleum drilling, powder processing, and slurry concentration, and have more recently been adopted in dust collection systems [1–4]. A typical hydrocyclone comprises a cylindrical body, a

conical section, a centrally positioned overflow outlet at the top, and an underflow outlet at the base [5]. This straightforward design enables cost-effective manufacturing while supporting the handling of large flow rates [6]. The flow inside a hydrocyclone is dominated by two distinct vortex patterns: the primary vortex, which spirals downward along the outer region, and the secondary vortex, which moves upward along the central axis [7,8]. When a suspension containing solid particles enters through the tangential inlet, it traverses the cylindrical and conical regions, where a high-intensity centrifugal field is generated. This force directs the denser particles toward the wall, leading to their discharge through the underflow, while finer particles and the carrier fluid are drawn toward the negative-pressure core, creating an upward spiral that exits through the overflow. The efficiency of particle separation is influenced by multiple interrelated factors, including the particle dimensions, density contrast, inlet velocity, and turbulence characteristics [9,10].

Hydrocyclone research has long focused on understanding how geometry and operating conditions shape the internal flow field and particle separation [11]. Experimental and computational approaches have demonstrated that relatively small design alterations can lead to significant differences in the mass split, pressure distribution, and separation efficiency [12,13]. One notable contribution is that of Vieira and Barrozo, who proposed a filtering-type hydrocyclone by replacing the conventional conical wall with a porous surface [14]. Their study, supported by both laboratory tests and CFD analysis, revealed that reducing the vortex finder diameter intensified the underflow discharge but increased the pressure drop. Enlarging the diameter, in contrast, lowered the fine particle recovery while concentrating solids in the underflow. These findings demonstrated how overflow geometry governs both the hydraulic performance and solids partitioning. Zhang et al. [15] investigated fine particle loss caused by short-flow near the vortex finder. They incorporated microchannels into the overflow structure of a mini-hydrocyclone to suppress this phenomenon. Their results show a reduction in short-flow intensity by nearly 94% and microplastic removal efficiencies above 98% for small polymethyl methacrylate particles. This highlights the potential of local outlet modifications to substantially limit undesired particle escape, even under low-density, low-loading conditions. Fang et al. [16] investigated the breakup of weakly cemented gas-hydrate-bearing sediments under hydrocyclone action. By introducing a rotational motion force model for aggregated particles and validating it through computational fluid dynamics discrete element method coupled simulations and experiments, they linked the macroscopic geometry and operating conditions to microscopic de-cementation processes. Their findings emphasize that the cone geometry and residence time in the cylindrical section are decisive factors in aggregate disintegration. Guo et al. [17] explored the role of the inlet velocity in bioengineering applications of hydrocyclones, specifically for separating aerobic granular sludge. Using both experiments and RSM turbulence modelling with particle tracking, they identified an optimal range of inlet speeds that maximized dense granule recovery while avoiding excessive pressure loss. The study confirmed that centrifugal forces and tangential shear must be balanced against energy costs. Xu et al. [18] examined how the ratio between the vortex finder diameter and the spigot diameter influences the development of the air core. Their simulations revealed that when this ratio becomes small, the central air column shortens and becomes less stable, indicating that the overflow configuration can strongly affect the formation of core structures and the resulting pressure field. This work highlighted that the outlet geometry does far more than control the discharge area; it plays a central role in shaping the internal vortex system. Zhang et al. [19] studied the impact of modifying both the size and the insertion depth of the vortex finder. They reported that increasing the vortex-finder diameter strengthens the upward discharge and increases the proportion of fluid leaving through the overflow, while simultaneously allowing a greater number of

fine particles to escape. Conversely, deeper insertion distorted the core flow and intensified short-circuiting, which ultimately reduced the separation efficiency. Their findings emphasized that the geometry near the overflow governs not only the trajectory of fine particles but also the stability of the upward vortex. More recently, Liu et al. [20] explored hydrocyclones featuring two cylindrical sections with different height ratios. Their results demonstrate that extending the upper cylindrical section increased the residence time and significantly lowered the cut size from roughly 93 μm to approximately 76 μm, which translated into better fine-particle separation. They also noted that certain height ratios reduced the misplacement of near-cut particles, underscoring the importance of axial length in controlling separation behavior. Their study made clear that adjusting the axial geometry offers a viable path to improving the removal of finer solids.

Taken together, these investigations underline three consistent observations. First, even minor adjustments in geometry—whether in the vortex finder, cone profile, or outlet details—can alter the vortex structure and particle pathways in complex ways. Second, particle-scale phenomena, such as cohesion loss, inertial migration, and drag–centrifugal force balance, are tightly coupled to these geometric changes. Third, the selection of operating parameters interacts with the geometry, producing trade-offs between the separation efficiency and hydraulic losses. Building on these insights, the present work examines the effects of the overflow diameter and cone length on hydrocyclone performance. We aimed to enhance our understanding of how various geometric parameters influence the core vortex system and the separation paths of particles by integrating detailed flow-field diagnostics with particle tracking for multiple particle sizes. This study highlights that the diameter ratio is crucial in forming the foundational vortex structure. In contrast, the aspect ratio amplifies this effect by improving the particle residence time and vortex persistence. This reveals a synergistic interaction between the two parameters rather than a simple additive effect, which aids in identifying configurations that enhance the removal of fine particles.

2. Numerical Methodology

2.1. Numerical Cases

This study investigated the effects of two geometric parameters of a hydrocyclone, namely, the diameter and aspect ratios, through numerical analysis. Seven configurations were considered for comparison, with the main dimensions and specifications summarized in Figure 1 and Table 1. In every case, the inlet diameter (D_i) was fixed at 28 mm. The diameter ratio (D_o/D_c) refers to the ratio of the overflow pipe (vortex finder) diameter (D_o) to that of the cylindrical section diameter (D_c), which is the short cylindrical region located at the upper part of the cyclone, directly connected to the tangential inlet and the conical section. For the comparison with different diameter ratios (Table 1), five numerical cases were considered. The diameter ratios were 0.23, 0.3, 0.37, 0.45, and 0.47 in Cases 1–5, respectively. When this ratio is reduced, the volume of the central vortex region becomes smaller, leading to an increase in the core flow velocity and a higher probability that fine particles will be carried toward the underflow. However, if the ratio becomes too small, the resulting higher internal pressure losses and the potential for flow blockage may degrade performance.

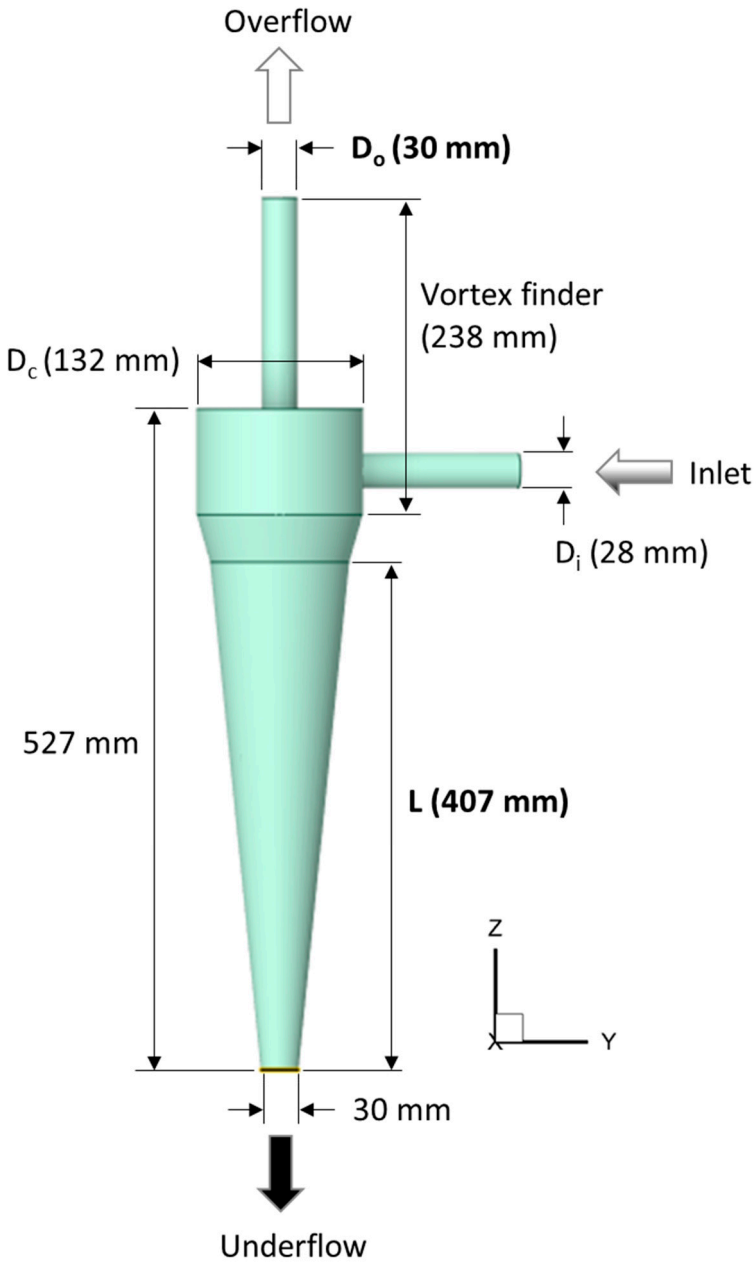


Figure 1. Schematic of the hydrocyclone with geometrical structure for Case 1.

Table 1. Geometric specifications of the hydrocyclone with different diameters (Cases 1–5) and aspect (Cases 5–7) ratios.

Model	Cylinder Diameter D_c (mm)	Overflow Diameter D_o (mm)	Diameter Ratio D_o/D_c	Aspect Ratio L/D_c	Length L (mm)
Case 1	132	30	0.23	3.0	396
Case 2	132	40	0.3	3.0	396
Case 3	132	50	0.37	3.0	396
Case 4	132	60	0.45	3.0	396
Case 5	132	62	0.47	3.0	396
Case 6	132	62	0.47	4.5	610
Case 7	132	62	0.47	6.0	814

For the comparison with different aspect ratios (Table 1), three numerical cases were considered. The aspect ratios (L/D_c) were 3, 4.5, and 6 in Cases 5–7, respectively. The aspect ratio is defined as the ratio of the conical section's axial length (L) to the diameter (D_c) of the cylindrical section. In this study, modifications to the aspect ratio were made

based on Case 5, as this configuration exhibited the most favorable distribution of flow between the overflow and underflow among Cases 1 to 5. By adopting Case 5 as a reference, subsequent changes in the cone length were used to assess how the aspect ratio influences the flow stability and particle separation. This parameter governs the residence time of the fluid and the degree to which the swirling flow develops. A larger aspect ratio generally lowers the likelihood of particles migrating toward the central axis, which can contribute to improved separation efficiency. The flow medium was a multiphase mixture of water, oil, and suspended solid particles. The total mass flow rate was set at 5880 kg/h, with an inlet temperature of 390 K, an operating pressure of 1296 kPa, and a fluid density of 938 kg/m^3. The boundary conditions included a mass flow inlet at the entry, non-slip reflective walls, a pressure outlet with particle escape at the overflow, and a pressure outlet with particle trapped at the underflow.

2.2. Experimental Validation and Grid Dependency

The computational domain was discretized into a grid using the finite volume method, allowing for the numerical simulation of the flow field. In this study, the numerical simulations of the hydrocyclone were validated against the experimental data originally reported by Dabir (1983) [21]. Dabir's work provides detailed measurements of velocity profiles and flow characteristics within a hydrocyclone, serving as a reliable benchmark for computational fluid dynamics (CFD) validation. The CFD results were compared with the experimental data, and Figure 2 illustrates the tangential velocity distributions at a vertical position of Z = 0.18 m and a Reynolds number of Re = 20,100, where good agreement was observed. Similar experimental validation was performed in the previous study [14]. These experimental validations demonstrate that the numerical model can accurately capture the complex swirling flow patterns and radial velocity variations inside the hydrocyclone, establishing confidence in the computational approach before proceeding to parametric studies.

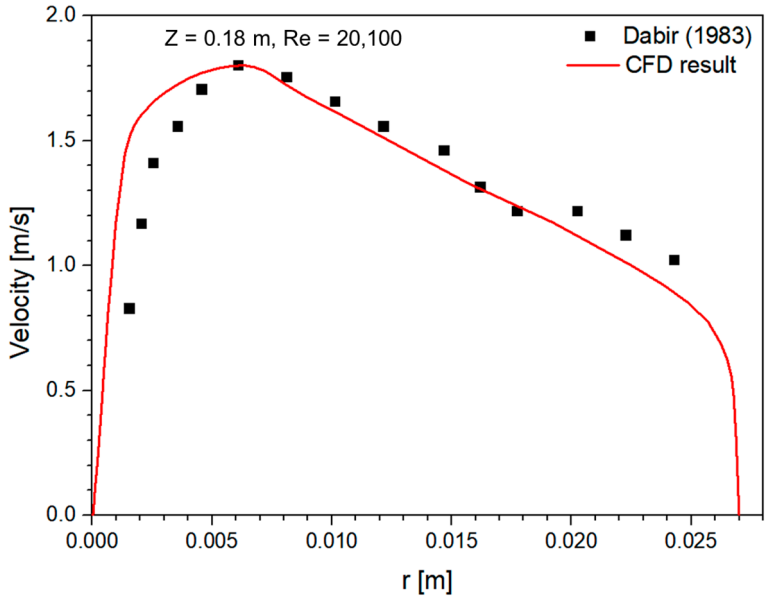


Figure 2. Tangential velocity profiles inside the hydrocyclone at Z = 0.18 m and Re = 20,100: comparison between CFD results and experimental data [14,21].

To verify the robustness of the numerical predictions, a mesh independence test was carried out using four computational grids with progressively refined resolutions in Case 1. The characteristic cell length was scaled using ratios of 1 (4 mm), 0.75 (3 mm), 0.5 (2 mm),

and 0.4 (1.6 mm), which corresponded to meshes that contained roughly 200,000, 400,000, 1,200,000, and 2,100,000 cells. In each case, the domain geometry was kept identical, while only the cell size was adjusted, which allowed for a systematic examination of the sensitivity of the results to grid density. All simulations were performed under the same operating and boundary conditions. The comparison focused on radial velocity profiles obtained along the axial position 0.28 m below the vortex finder, near the entrance of the conical section. This region was chosen because it contains strong velocity gradients and the development of the swirling core, making it particularly suitable for assessing mesh resolution effects. In Figure 3, the results indicated that the two coarse grids (200,000 and 400,000 cells) produced radial velocity fields that differed significantly from those predicted by the two fine grids. This confirmed that such coarse meshes were inadequate for resolving the flow characteristics inside the hydrocyclone. In contrast, the 1,200,000-cell grid produced velocity distributions very close to those from the 2,100,000-cell grid, suggesting that grid convergence had effectively been reached at this resolution. In addition to comparing velocities, we also assessed the pressure drop across the hydrocyclone as an additional metric for mesh sensitivity (Figure 4). The predicted pressure drops for characteristic cell lengths of 4, 3, 2, and 1.6 mm were 28,655, 29,706, 32,316, and 32,603 Pa, respectively. While the coarse meshes showed significant deviations from the finest grid, the pressure drop calculated with the 1,200,000-cell mesh differed by less than 1% from that of the 2,100,000-cell mesh. This close agreement further confirms that a mesh resolution of 2 mm provides adequate numerical accuracy for flow-field predictions and hydraulic performance indicators, and thus, was adopted for the mesh generation across most cases. Consequently, the meshes for Cases 1 to 3 comprised approximately 1,200,000 cells each, while Case 4 comprised about 1,650,000 cells, and Case 5 contained roughly 1,780,000 cells; Cases 6 and 7 were discretized with approximately 1,800,000 and 2,000,000 cells, respectively, reflecting a gradual increase in the grid resolution to capture finer flow details. These resolutions provided a practical balance between computational efficiency and numerical fidelity, ensuring that the primary and secondary vortex structures and the associated velocity distributions were captured with sufficient accuracy for meaningful analysis. Figure 5 presents a visualization of the mesh configuration for Case 7.

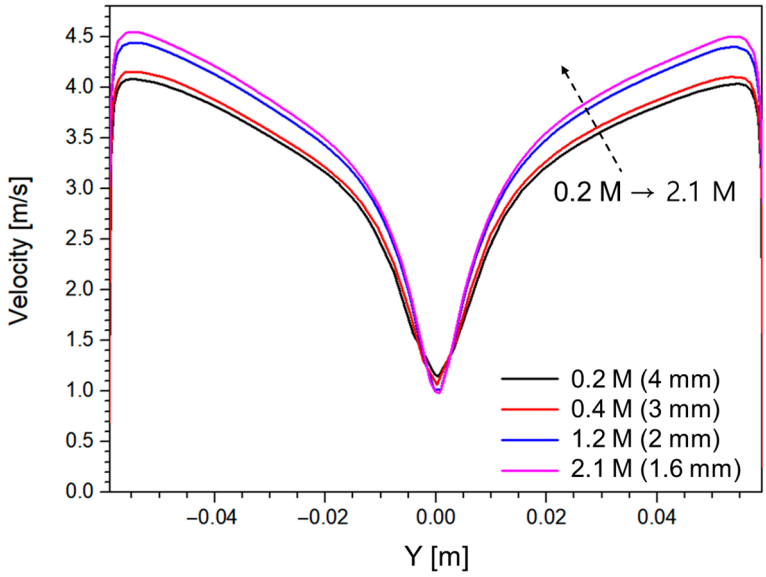


Figure 3. Velocity magnitude distributions with different mesh sizes (4, 3, 2, and 1.6 mm) for Case 1.

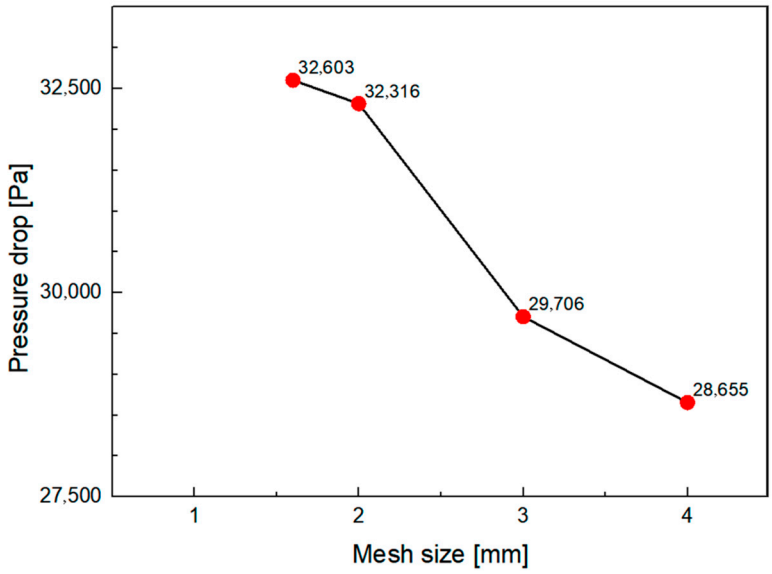


Figure 4. Pressure drop variations with different mesh sizes (4, 3, 2, and 1.6 mm) for Case 1.

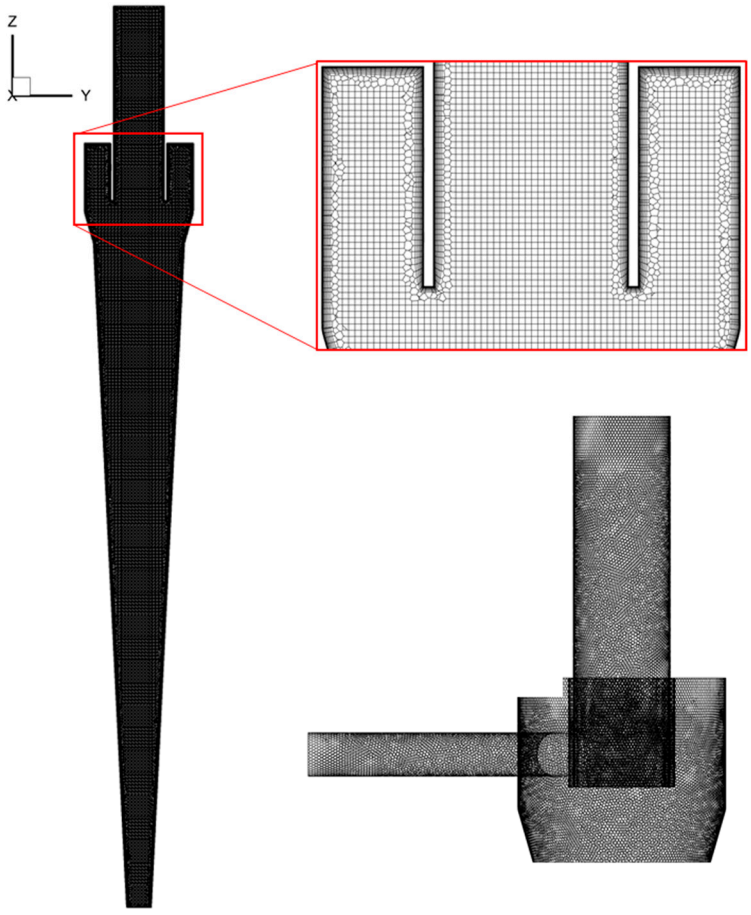


Figure 5. Mesh generation of the hydrocyclone separator in Case 1.

2.3. Numerical Models

In this study, a steady-state numerical simulation was performed to investigate the three-dimensional flow field and particle motion within the hydrocyclone. The computations were carried out using ANSYS Fluent 2022 R2 (ANSYS, Inc., Canonsburg, PA, USA). Pressure-velocity coupling was achieved through the SIMPLE algorithm. As the primary focus was on the free-shear flow behavior rather than near-wall effects, the *k*-*ε* turbulence

model was selected. To more accurately represent the pronounced swirling motion and vortex structures inside the cyclone, the realizable *k*-ε was employed [22,23]. The general governing equations are as follows:

Mass conservation equation:

$$\frac{\partial}{\partial x_i}(\rho v_i) = 0 \tag{1}$$

Momentum conservation equation:

$$\frac{\partial}{\partial x_j}(\rho v_i v_j) = -\frac{\partial p}{\partial x_i} + \frac{\partial \bar{\bar{\tau}}_{ij}}{\partial x_j} + \rho g_i \tag{2}$$

Energy equation:

$$\frac{\partial}{\partial x_i}[u_i(\rho E + p)] = \frac{\partial}{\partial x_j}\left(k_{eff}\frac{\partial T}{\partial x_j} + u_i(\tau_{ij})_{eff}\right) + S_h \tag{3}$$

Realizable *k*-epsilon model equation:

$$\frac{\partial}{\partial x_j}(\rho k u_j) = \frac{\partial}{\partial x_j}\left[\left(\mu + \frac{\mu_t}{\sigma_k}\right)\frac{\partial k}{\partial x_j}\right] + G_k - \rho\varepsilon \tag{4}$$

$$\frac{\partial}{\partial x_j}(\rho \varepsilon u_j) = \frac{\partial}{\partial x_j}\left[\left(\mu + \frac{\mu_t}{\sigma_\varepsilon}\right)\frac{\partial \varepsilon}{\partial x_j}\right] + \rho C_1 S_\varepsilon - \rho C_2 \frac{\varepsilon^2}{k + \sqrt{v\varepsilon}} + C_{1\varepsilon}\frac{\varepsilon}{k}C_{3\varepsilon}G_b \tag{5}$$

Turbulent viscosity:

$$\mu = C_\mu \rho \frac{k^2}{\varepsilon} \tag{6}$$

The model constants have the following default values:

$$C_{1\varepsilon} = 1.44,\ C_{2\varepsilon} = 1.92,\ C_\mu = 0.09,\ \sigma_k = 1.0,\ \sigma_\varepsilon = 1.3 \tag{7}$$

Particle trajectories were resolved using the discrete phase model, which enables the explicit tracking of individual solid-phase particles relative to the continuous fluid phase while accounting for relevant forces such as drag, gravity, and turbulence interactions. Fluent predicts the trajectory of a discrete phase particle by integrating the force balance on the particle, which is written in a Lagrangian reference frame. This force balance equates the particle inertia with the forces acting on the particle and can be written as follows:

$$\frac{\boldsymbol{du_p}}{\boldsymbol{dt}} = \boldsymbol{F_D}(\boldsymbol{u} - \boldsymbol{u_p}) + \frac{\boldsymbol{g_x}(\boldsymbol{\rho_p} - \boldsymbol{\rho})}{\boldsymbol{\rho_p}} + \boldsymbol{F_x} \tag{8}$$

where F_x represents an additional acceleration term, while the other two terms on the right-hand side correspond to the drag force (F_D) and gravitational force (g_x), respectively. This formulation allows the model to capture the trajectory and residence time of each particle in complex flow fields [24].

To describe the particle size distribution, the Rosin–Rammler expression was employed, which is commonly used to represent polydisperse droplets or solid particles generated from comminution processes. The full range of particle sizes is divided into discrete intervals, with each interval represented by a mean particle diameter for which

trajectory calculations are performed. For a Rosin–Rammler distribution, the mass fraction of particles with diameters greater than d is given by

$$Y_d = \exp\left[-\left(\frac{d}{d_m}\right)^n\right] \quad (9)$$

where d_m is the mean diameter and n is the spread parameter that describes the uniformity of particle sizes. This formulation allows for a realistic representation of the particle size variation, enabling the accurate simulation of particle trajectories and separation behavior in the flow field. To model the particulate phase, solid particles representing stone, with a density of 2800 g/cm^3, were introduced through the inlet surface. The particle feed rate was set to 1% of the total mass flow, which corresponded to 63 kg/h. Four representative particle sizes—10, 30, 50, and 100 µm in diameter—were injected to assess the particle size's impact on the separation behavior.

3. Results and Discussion

3.1. Effect of Diameter Ratio

Figures 6a and 6b show the internal pressure and axial velocity distributions, respectively, with different diameter ratios (0.23, 0.3, 0.37, 0.45, and 0.47 for Cases 1–5, respectively). For Case 1 (shown in Figure 6), which exhibits the smallest diameter ratio, the discharge of fluid through the upper outlet could be restricted even under constant inlet flow conditions. This is due to the formation of a high-speed axial jet inside the vortex finder, driven by the fluid converging strongly toward the center to pass through the narrow outlet (Figure 6b). Furthermore, the reduced diameter of the vortex finder diminishes the fluid discharge capacity at the cone region, thereby decreasing the magnitude of the axial negative pressure (shown in Figure 6a) and degrading the pressure gradient near the axis. This trend is clearly observed in the pressure contours of Case 1, where the low-pressure region at the center is significantly weakened.

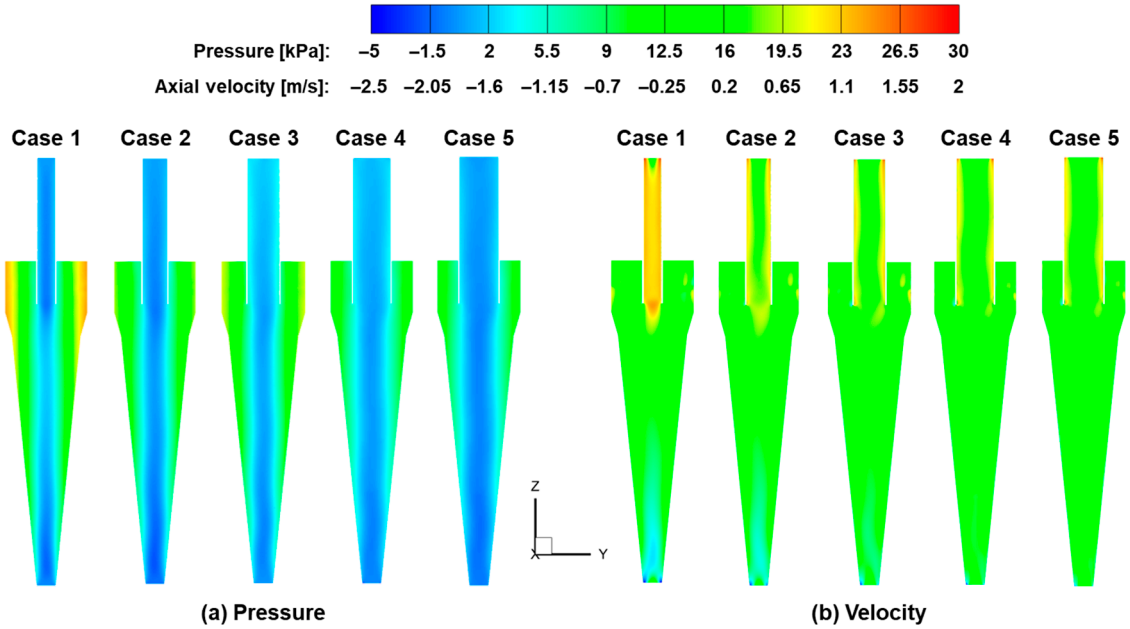


Figure 6. Pressure (**a**) and velocity (**b**) contours on vertical section with different diameter ratios (0.23, 0.3, 0.37, 0.45, and 0.47 for Cases 1–5, respectively).

Figures 7 and 8 show the distribution of axial velocity along the centerline and the discharge ratio of flow rates in terms of the upper and lower flows relative to the inlet

flow (total flow), respectively, with different diameter ratios. Compared to configurations with larger diameter ratios, a reduction in this ratio increases the axial velocity shown in Figure 7 near the upper outlet; however, the total fluid volume discharged upward decreases (Figure 8). In particular, when contrasted with Case 5, Case 1 exhibits a markedly reduced low-pressure region, as shown in Figure 6a, and a diminished influence of the secondary vortex due to the narrower vortex finder diameter (Figure 9). As a result, nearly 63% of the total flow of Case 1 shown in Figure 8 is discharged through the lower outlet instead of being evenly split. As the diameter ratio increases across the cases, the low-pressure region dominated by the secondary vortex expands relative to Case 1, promoting stronger upward flow and increasing the fraction of fluid exiting through the upper outlet. Although the axial velocity near the vortex finder remains nearly constant in most cases, the downward velocity near the bottom section is greater in the smaller-diameter-ratio cases, which explains the observed shift in the overall flow distribution.

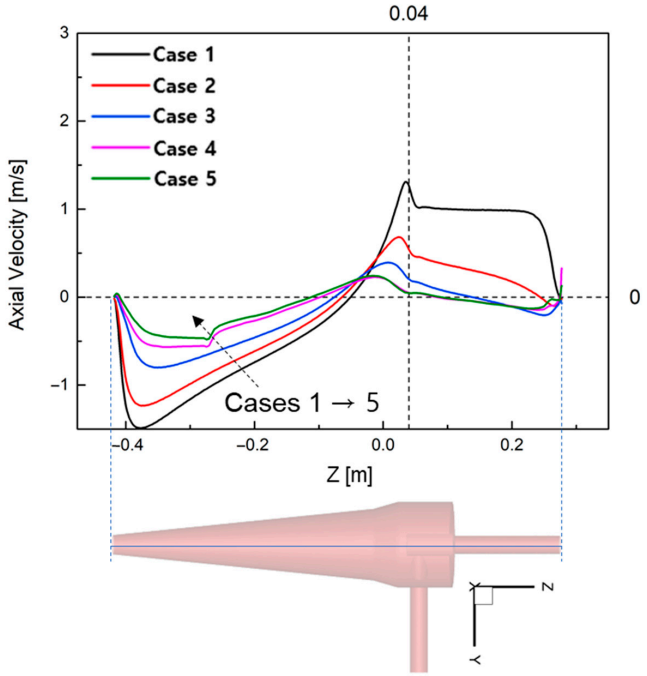


Figure 7. Distributions of axial velocity along a vertical line with different diameter ratios (0.23, 0.3, 0.37, 0.45, and 0.47 for Cases 1–5, respectively).

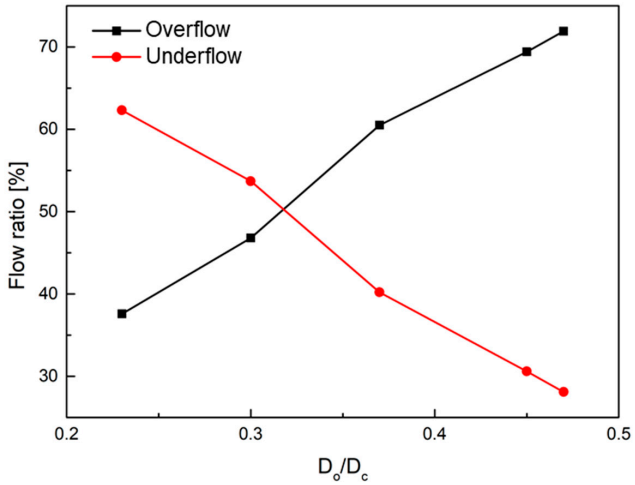


Figure 8. Flow ratios (flow ratio at overflow = overflow/total flow, total flow = overflow + underflow) for different diameter ratios (0.23, 0.3, 0.37, 0.45, and 0.47 for Cases 1–5, respectively).

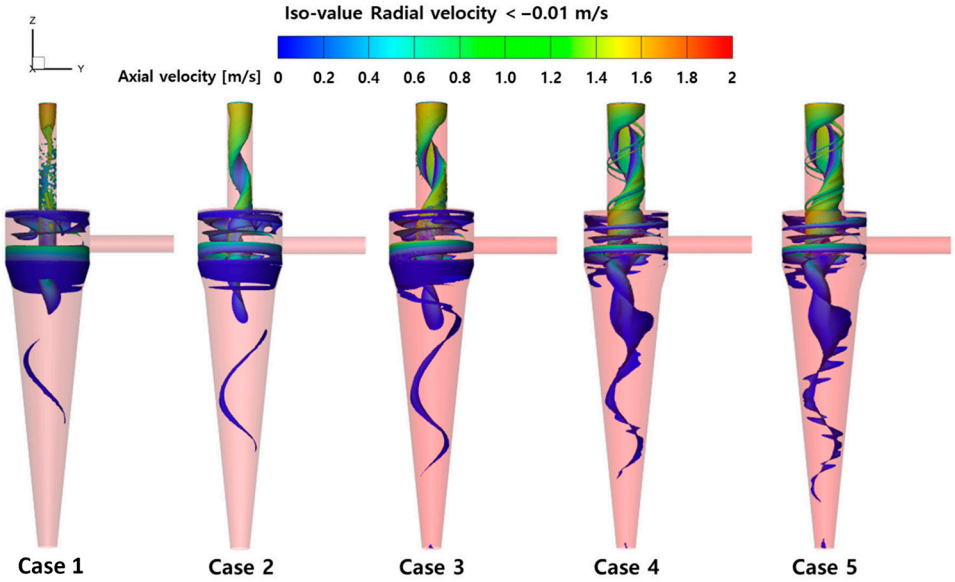


Figure 9. Secondary vortex structures using iso-value at radial velocity less than −0.01 m/s with axial velocity represented by color for different diameter ratios (0.23, 0.3, 0.37, 0.45, and 0.47 for Cases 1–5, respectively).

In Figure 9, the radial velocity analysis provided a direct means to evaluate how much of the surrounding flow contributes to the upward motion sustained by the secondary vortex. For this purpose, Figure 9 illustrates the radial inflow region, defined as the zone where the radial velocity was less than −0.01 m/s. The threshold of −0.01 m/s was deliberately selected, rather than zero, to emphasize areas of appreciable inward motion toward the axis, thereby including values such as −0.02 or −0.03 m/s that indicate stronger radial inflow. In Case 1, the radial inflow region extends across much of the cylindrical section, while the upward transport through the core toward the overflow remains limited. As the diameter ratio increases, the radial inflow region associated with the secondary vortex expands, strengthening the upward flow and increasing the proportion of fluid discharged through the vortex finder. This finding is consistent with the discharge flow ratios presented in Figure 8. The trends in pressure drop provide further insights into the hydraulic effects of varying the diameter ratio (Figure 10). As the diameter ratio increases from 0.25 to 0.3, the pressure drop decreases significantly, falling from 32,316 to 22,286 Pa. This indicates that very small openings of the vortex finder create strong flow confinement, which hinders the stable development of the secondary vortex. When the diameter ratio exceeds approximately 0.37, the pressure drop decreases more gradually (from 20,976 to 17,321 to 16,294 Pa), suggesting a transition to a more stable core structure and reduced hydraulic losses. These findings confirm that excessively small diameter ratios lead to unnecessary energy penalties and restrict upward flow, while moderate-to-large diameter ratios offer more stable overflow behavior and lower pressure drop requirements. These results can also be explained using quantitative force balance expressions. The motion of particles within a hydrocyclone is governed by the centrifugal force, drag force, gravitational force, and buoyancy. Among these, gravity and buoyancy act in the axial direction and are typically negligible in magnitude. Thus, this study primarily focused on the effects of the centrifugal and drag forces. The force balance acting on a particle in the hydrocyclone is represented schematically in Figure 11.

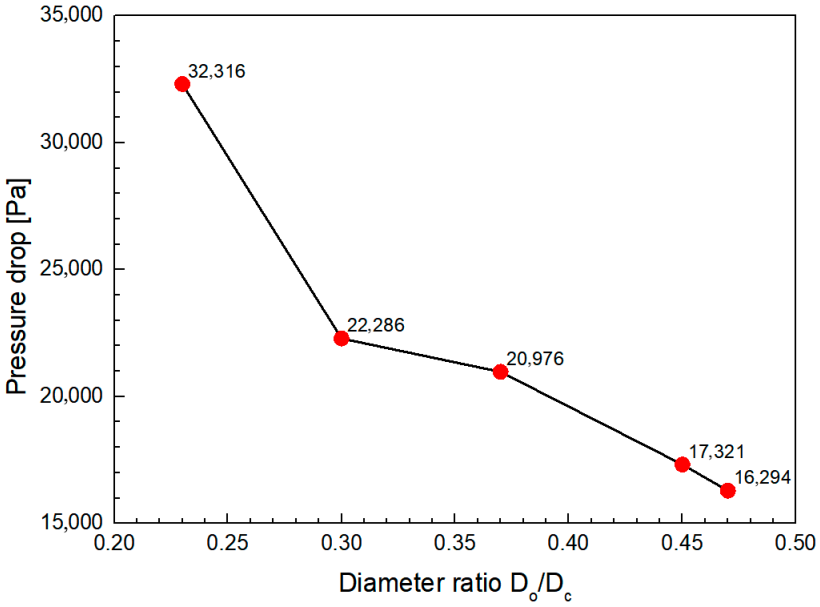


Figure 10. Pressure drop as a function of the diameter ratio (D_o/D_c).

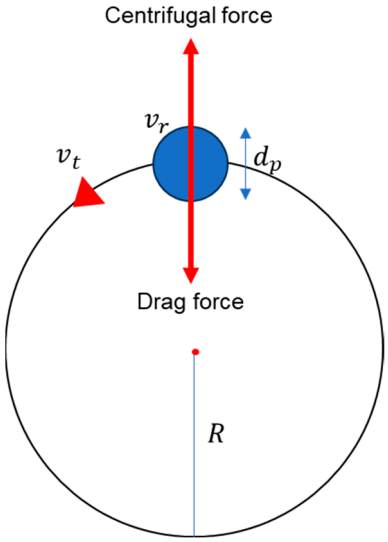


Figure 11. Schematic of particle force on radial section.

The particle motion inside the hydrocyclone is mainly governed by centrifugal and drag forces acting in the radial direction. The centrifugal force arises from the particle's rotational motion and can be expressed as follows:

$$\rho_p \frac{\pi}{6} d_p^3 \frac{v_t^2}{R} \tag{10}$$

where ρ_p is the particle density (kg/m^3), d_p is the particle diameter (m), v_t is the tangential velocity of the particle (m/s), and R is the radial distance (m) from the cyclone axis.

The drag force, which resists the particle's motion relative to the surrounding fluid, is given by:

$$3\pi\mu d_p v_r \tag{11}$$

where μ is the dynamic viscosity of the fluid (Pa·s) and v_r is the relative velocity (m/s) between the fluid and the particle in the radial direction.

In this analysis, the balance between the centrifugal and drag forces determines whether particles move outward toward the wall or inward toward the central core, con-

sistent with the equilibrium orbit theory described by Hsieh and Rajamani [25]. Particles experiencing a dominant centrifugal force tend to follow the outer vortex and exit through the underflow, while those more strongly affected by drag are entrained into the secondary vortex and carried upward to the overflow. The relative magnitudes of these forces depend primarily on the particle size, the density difference between phases, and local flow velocity within the cyclone. Figure 9 shows that increasing the diameter of the vortex finder leads to an increase in the upward discharge flow rate. This observation is consistent with the findings of Wu et al. [26], who reported that a reduction in the tangential velocity within the hydrocyclone weakens the centrifugal force, thereby promoting particle migration toward the central core and increasing the proportion of flow discharged through the overflow. This relationship is clearly evident in Figure 12, which presents the tangential velocity distribution at a position 0.28 m downstream from the top of the hydrocyclone. The graph shows a decreasing trend in tangential velocity with increasing diameter ratio. As the tangential velocity diminishes, the reduced centrifugal force allows more particles to enter the secondary vortex and be discharged through the overflow, which may lead to a reduction in the overall separation efficiency. Figure 13 provides a quantitative analysis of the particle separation efficiency as a function of both the diameter ratio and particle size. The results indicate that as the particle diameter decreases, drag becomes more influential, leading to a greater proportion of particles being transported upward along the secondary vortex and discharged through the overflow. While particles larger than 50 μm maintained a separation efficiency above 80% at higher diameter ratios, smaller particles exhibited a significant decrease in separation efficiency. These findings underscore the need for design modifications to improve the separation of fine particles.

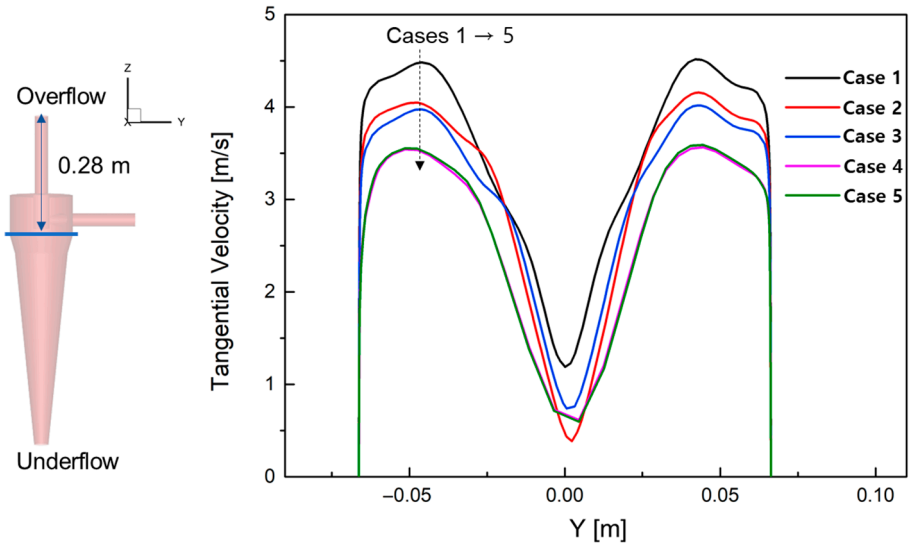


Figure 12. Tangential velocity distributions for different diameter ratios (0.23, 0.3, 0.37, 0.45, and 0.47 for Cases 1–5, respectively) obtained at 0.28 m from the top of the vortex finder's surface.

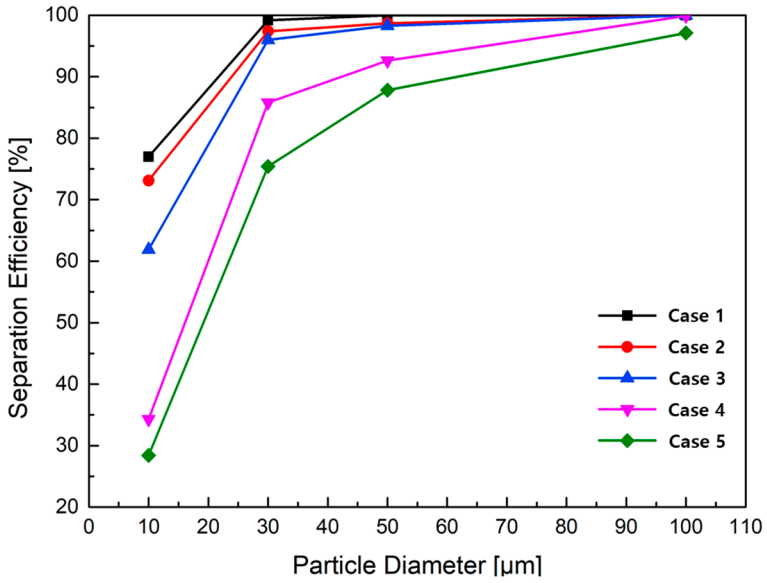


Figure 13. Separation efficiency of particles with different diameter ratios (0.23, 0.3, 0.37, 0.45, and 0.47 for Cases 1–5, respectively).

3.2. Effect of Aspect Ratio

Based on the results regarding the diameter ratio effect, a reduction in the vortex finder diameter and corresponding diameter ratio was found to enhance the downward particle separation. While this effect is beneficial from a particle separation standpoint, it also led to the undesired outcome of fluid being discharged along with the particles through the underflow, thereby reducing the overall efficiency of the upward separation. As a result, although the particle removal was improved, the overall flow separation performance was suboptimal. To address this limitation, the present study introduced structural modification by varying the aspect ratio, defined as the ratio of the cone length to the cylinder diameter. A similar study was performed by Fu et al. [27], who demonstrated that modifications to the conical section geometry, such as varying the cone angle, can substantially influence the separation performance. In this study, starting from Case 5, which exhibited the most favorable upward flow discharge among the previous configurations, new cases were generated by incrementally increasing the aspect ratio. Figure 14 presents the pressure contours for Cases 5–7 corresponding to different aspect ratios. The results indicate that increasing the aspect ratio did not lead to abnormal reductions in the central negative pressure or excessive increases in the pressure within the cylinder section. Rather, the overall pressure gradient remained consistent, suggesting that the modified geometry does not adversely affect the formation of a stable flow field.

The aspect ratio's impact on the flow distribution was investigated by comparing the discharge flow rates at the upper and lower outlets (Figure 15). While the general discharge trend remained consistent, an increase in the aspect ratio from 3.0 to 4.5 led to a slight rise in the upward discharge. However, when the aspect ratio was further increased to 6.0, the change in flow distribution was minimal, suggesting that beyond a certain threshold, additional increases in the cone length have a limited effect on the flow separation. Figure 16 presents the axial velocity distribution, indicating that an increase in the aspect ratio results in a longer region of upward flow formation and a more stabilized and coherent flow structure. Figure 17 visualizes the central converging flow by highlighting areas with radial velocity less than -0.01 m/s. The results demonstrate that the convergence zone expanded with increasing aspect ratio, thereby strengthening the secondary vortex and contributing to an enhanced upward flow. The elongation of the conical section resulted in a more

gradual reduction in the cross-sectional area. In cyclones with a lower aspect ratio, the rapid decrease in radius forces the fluid to turn inward abruptly, which creates intense shear and results in a compressed, unstable vortex structure. In contrast, a larger aspect ratio allows the tangential flow to transition into inward radial flow more smoothly over a longer axial distance. This smooth transition reduces the radial velocity gradient, enabling the secondary vortex, which acts as a buffer zone for particle separation, to expand axially and stabilize. This stabilization of the upward flow with increased aspect ratio is consistent with the secondary vortex persistence analysis reported by Wang [28] and the hydrodynamic evaluations by Cavalcante et al. [29], both of whom noted that an elongated conical section can prolong and stabilize the upward vortex structure. Figure 18 shows that the pressure drop response provides further evidence of the hydraulic function of cone elongation. As the aspect ratio increased from 3 to 4.5 and then to 6, the pressure drop decreased nearly linearly—from 16,294 to 13,960 Pa and ultimately to 11,937 Pa. This trend suggests that a longer cone allows for a gentler axial deceleration, which reduces the energy losses while maintaining a stable upward core over a greater axial distance. These findings complement the separation results, demonstrating that larger aspect ratios improve the exposure time of fine particles to centrifugal forces, even when their effect on the overall flow split becomes less significant. Particle separation efficiency under varying aspect ratios is presented in Figure 19. The removal efficiency was found to improve for smaller particles as the aspect ratio increased. This can be attributed to the prolonged residence time within the cyclone, which allows for greater rotational motion and, consequently, stronger centrifugal effects. The stabilized secondary vortex depicted in Figure 17 plays a critical role in preventing re-entrainment of particles. This is visually supported by the contour diagrams, which show that disordered flow disturbances near the spigot—particularly evident in cases with a low aspect ratio—were noticeably suppressed as the aspect ratio increased. In short cone configurations, these turbulent fluctuations can unintentionally disturb separated particles, causing them to be reintroduced into the upward flow. However, in high aspect ratio cases, the expanded and coherent vortex structure acts as a hydrodynamic barrier, ensuring that particles settled near the wall continue on a downward path. This mechanism effectively maximizes the collection efficiency. As a result, denser particles are more likely to be forced toward the wall before they can enter the core region, making them more prone to be discharged downward. Additionally, the elongated conical section stabilizes the upward flow, as observed in Figures 16 and 17, thereby promoting greater fluid discharge through the overflow. Ultimately, the increase in aspect ratio led to concurrent improvements in the particle separation efficiency and flow separation performance.

The trends described above collectively clarify the physical origin of the efficiency trade-off observed in this study. The diameter ratio primarily regulates the competition between the outer primary vortex and the upward secondary vortex: when the vortex finder is narrow, strong centrifugal forcing dominates the flow field and drives particles—particularly coarse ones—outward toward the wall, but the weakened secondary vortex limits the amount of fluid that can be conveyed upward in a stable manner. As the diameter ratio increases, the outward centrifugal dominance diminishes, the low-pressure core expands, and the strengthened secondary vortex promotes a larger overflow, although the reduction in tangential velocity allows fine particles to drift inward under drag-dominated conditions and escape with the overflow. In contrast, variations in the aspect ratio influence the separation behavior primarily through residence-time control. A longer cone sustains the secondary vortex over a greater axial distance, allowing even small particles to experience the swirling field for a longer duration. This explains why cone elongation enhances the collection of fine particles, even when its impact on the bulk flow split becomes limited.

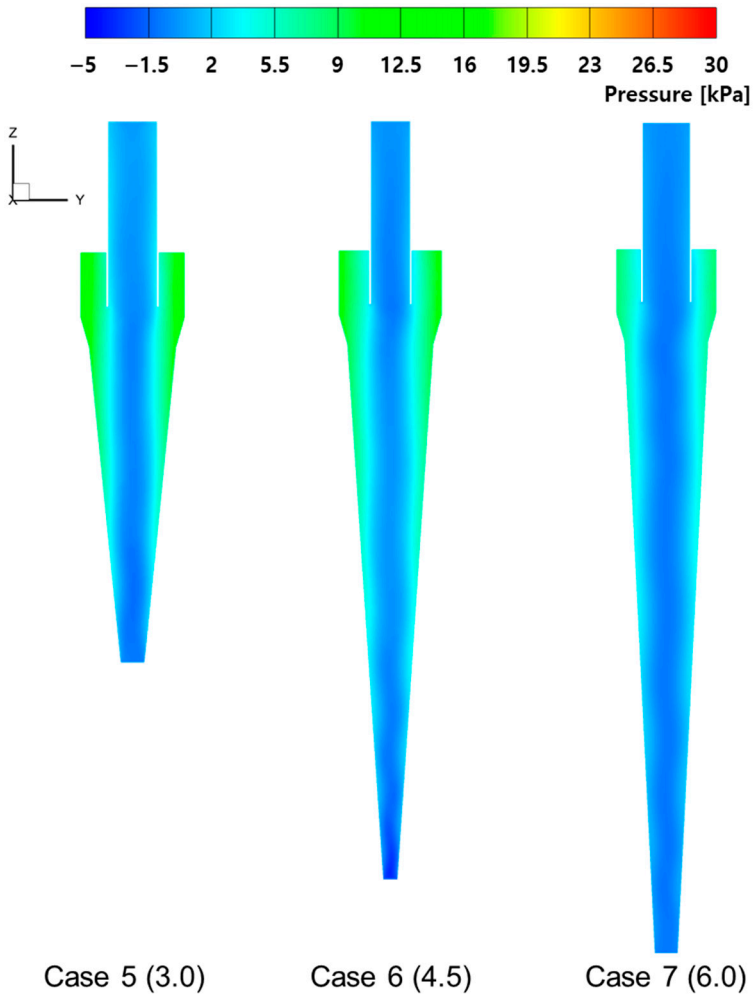


Figure 14. Pressure contours on vertical section with different aspect ratios (3, 4.5, and 6 for Cases 5–7, respectively).

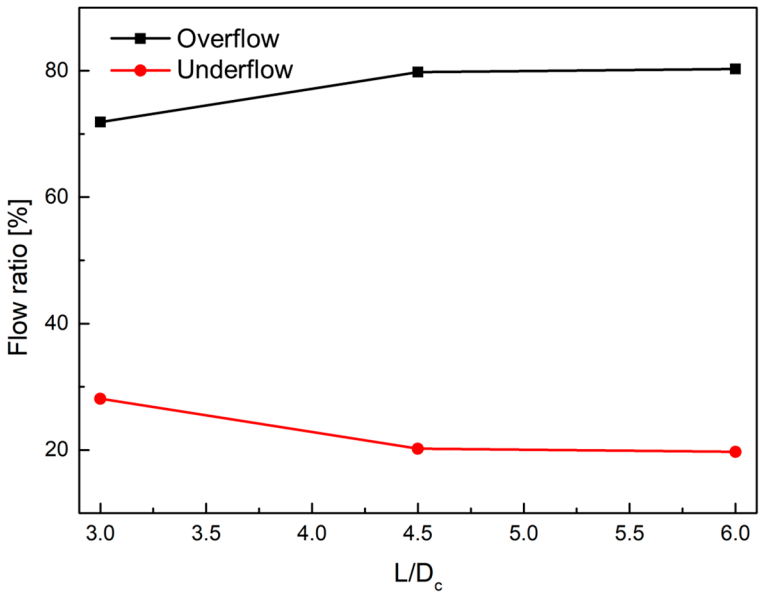


Figure 15. Flow ratios (flow ratio at overflow = overflow/total flow, total flow = overflow + underflow) in comparison with different aspect ratios (3, 4.5, and 6 for Cases 5–7, respectively).

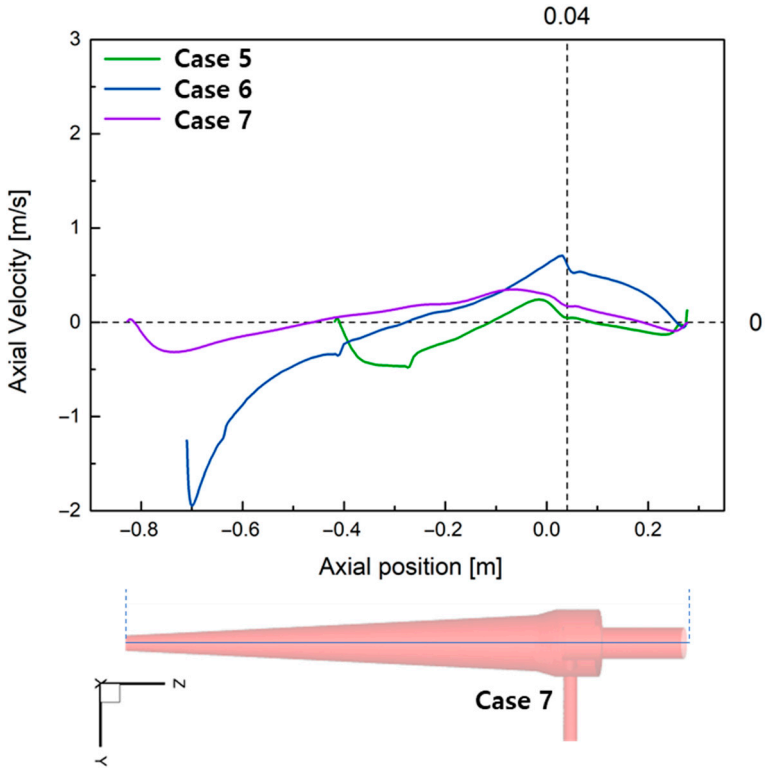


Figure 16. Distributions of axial velocity along a vertical line with different aspect ratios (3, 4.5, and 6 for Cases 5–7, respectively).

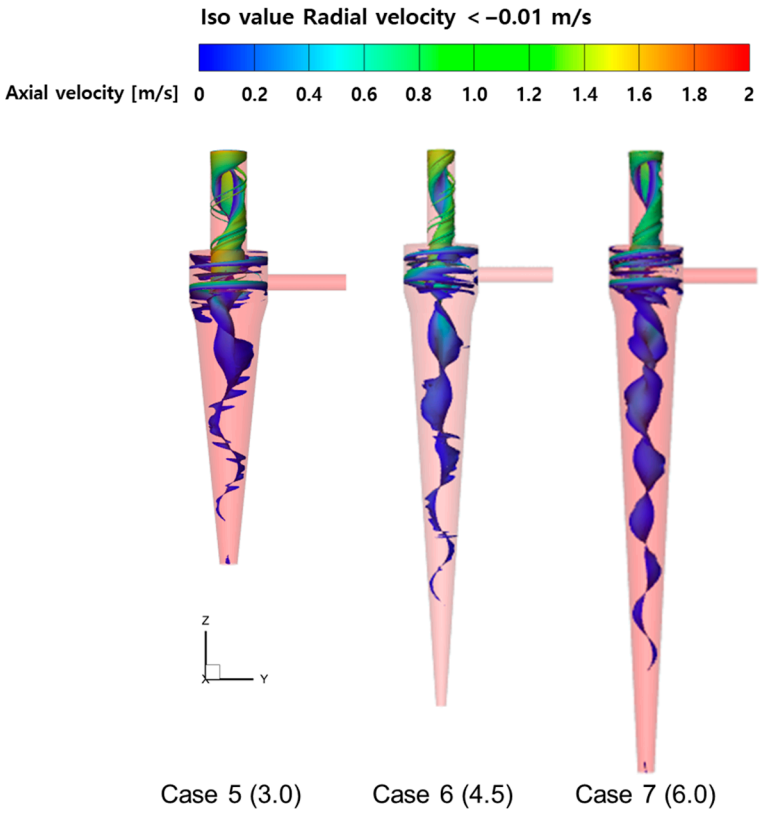


Figure 17. Secondary vortex structures using iso-value at radial velocity less than −0.01 m/s with axial velocity represented by color for different aspect ratios (3, 4.5, and 6 for Cases 5–7, respectively).

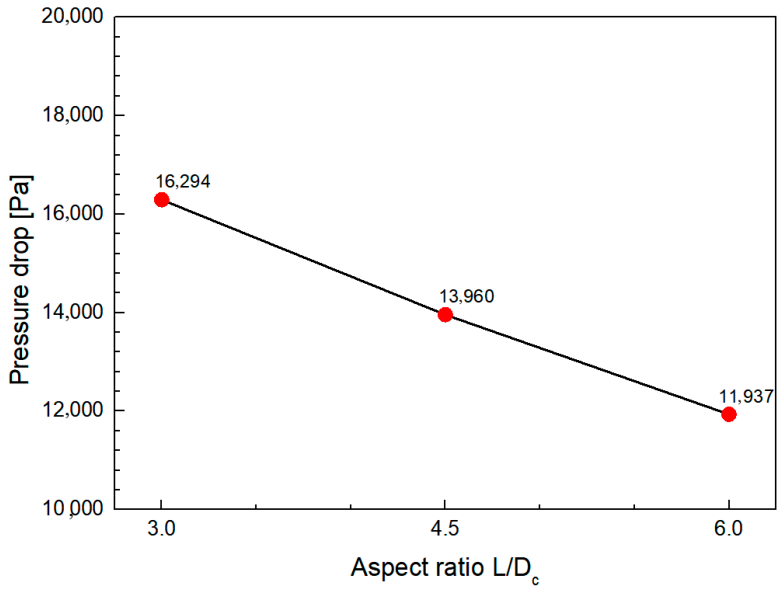


Figure 18. Pressure drop as a function of the aspect ratio (L/D_c).

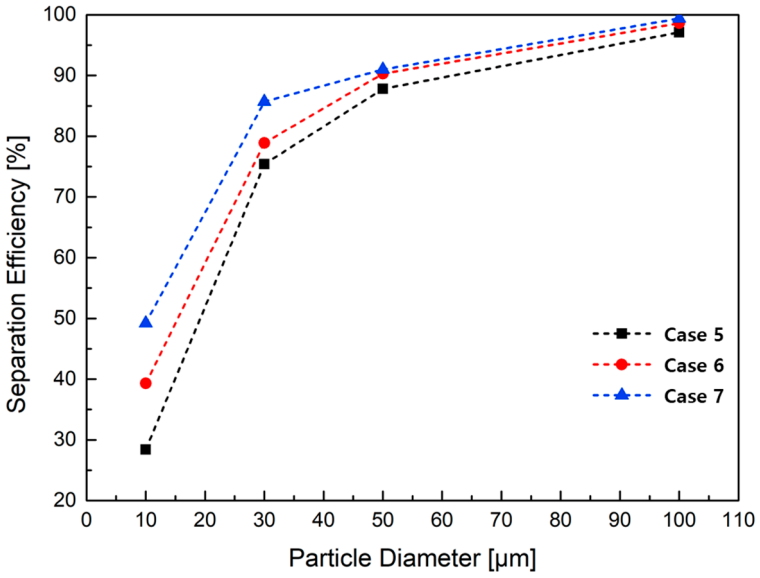


Figure 19. Separation efficiency of particles with different aspect ratios (3, 4.5, and 6 for Cases 5–7, respectively).

When combined, these results demonstrate that the two geometric parameters do not operate independently; rather, they function through a coupled mechanism. A sufficiently large diameter ratio creates a strong core region and a persistent secondary vortex. This, in turn, allows the elongated cone to enhance the stability of the upward vortex and extend the exposure of particles to centrifugal forces. In other words, the diameter ratio establishes the hydrodynamic conditions required for the beneficial effects of cone elongation to be fully realized, while the aspect ratio enhances the flow field structure influenced by the vortex finder. By clarifying how these interdependent roles influence the vortex strength, residence time, and forces acting on the particles, this study offers a coherent mechanistic explanation for the contrasting trends observed in overflow stability and fine-particle collection.

4. Conclusions

This study investigated how the vortex finder diameter and aspect ratios collectively influence the internal flow field and particle separation behavior of a hydrocyclone. Re-

ducing the diameter ratio enhanced the dominance of centrifugal forces in the outer vortex and increased the downward discharge of particles. Conversely, larger diameter ratios expanded the low-pressure core and led to an increase in the overflow discharge, reaching nearly 72% at the highest ratio. However, this increase was accompanied by a decrease in control over the motion of fine particles. These findings indicate that the diameter ratio primarily regulates the balance between centrifugal forces and inward transport toward the core, thus determining how the flow is divided between the underflow and overflow.

Adjusting the aspect ratio effectively addressed these tradeoffs. Increasing the length of the cone resulted in a longer particle residence time and stabilized the upward core flow, which improved the collection of fine particles. When the aspect ratio increased from approximately 3 to 4.5, the recovery rate of particles smaller than 30 μm rose by more than 10%, with further improvements observed as the ratio approached 6. Although this study examined only aspect ratios up to 6, the consistent gains suggest that the length of the cone primarily affects the time that particles are exposed to swirling forces, rather than changing the overall flow division.

The findings provide a clear understanding of the complementary roles played by different geometric parameters. The diameter ratio influences the relative strength of the primary and secondary vortex systems, which in turn affects the stability of overflow versus underflow discharge. Meanwhile, the aspect ratio acts as a tuning parameter based on the residence time, improving the capture of fine particles. To achieve stable overflow discharge, it is important to maintain a diameter ratio of at least 0.37, which allows for more than 60% of the total flow to be discharged as overflow. Additionally, using sufficiently large aspect ratios—preferably up to 6—can significantly enhance the collection of fine particles without destabilizing the flow. These insights provide a solid foundation for selecting geometric parameters based on specific industrial needs, whether the focus is on removing coarse solids, ensuring overflow clarity, or maximizing fine particle recovery.

Author Contributions: Conceptualization, S.A.; methodology, W.C.; software, D.S.; validation, S.C.; formal analysis, D.S.; investigation, D.S.; resources, Y.S.; data curation, W.C.; writing—original draft preparation, S.C.; writing—review and editing, Y.S.; visualization, W.C.; supervision, Y.S.; project administration, S.A.; funding acquisition, S.A. All authors have read and agreed to the published version of the manuscript.

Funding: This work is supported by the Ministry of Land, Infrastructure and Transport (MOLIT) and the Korea Agency for Infrastructure Technology Advancement (KAIA) (No. RS-2022-00142936).

Data Availability Statement: The original contributions presented in this study are included in the article. Further inquiries can be directed to the corresponding authors.

Conflicts of Interest: Seongyool Ahn was employed by the Institute for Advanced Engineering. The remaining authors declare that the research was conducted in the absence of any commercial or financial relationships that could be construed as a potential conflict of interest.

References

1. Knight, M.A.; Wates, J.A.; Du Plessis, I. Application of hydrocyclone technology to tailings storage facilities to reduce water consumption. In Proceedings of the 15th International Seminar on Paste and Thickened Tailings, Australian Centre for Geomechanics, Perth, Australia, 16–19 April 2012; pp. 233–241.
2. Zhang, Y.; Yang, M.; Jiang, L.; Wang, H.; Xu, J.; Yang, J. High Concentration Fine Particle Separation Performance in Hydrocyclones. *Minerals* **2021**, *11*, 307. [CrossRef]
3. Liu, P.; Gao, Z.; Yang, X.; Hou, D.; Jiang, L.; Jiang, Z.; Yan, Z. A study on the classification performance of water-injection hydrocyclone. *Physicochem. Probl. Mineral Process.* **2024**, *60*, 194539. [CrossRef]
4. Yang, X.; Yang, G.; Liu, P.; Li, X.; Jiang, L.; Zhang, J. Study on the Desliming Performance of a Novel Hydrocyclone Sand Washer. *Separations* **2022**, *9*, 74. [CrossRef]

5. Vimal, A.; Thalaieswaran, S.; Kannan, N.H.; Ganeshan, P.; Venkatesh, S. A review on the Investigation of Hydrocyclone Performance by shape optimization. *E3S Web Conf.* **2023**, *405*, 04047. [CrossRef]
6. Dhanorkar, M.; Mishra, I.; Sawant, R.; Sharma, K.; Sonawane, C.; Siddiqui, M.H.; Ashraf, I.; Tejani, G.G. Numerical simulation and experimental study of suspended particulate matter removal for efficient water recovery and reuse in solid–liquid separation. *Sci. Rep.* **2025**, *15*, 8060. [CrossRef]
7. Fernando, C.A.; Juan, L.B.A. Flow Pattern in Hydrocyclones. In *Fluid Mechanics Fundamentals of Hydrocyclones and Its Applications in the Mining Industry*; Fluid Mechanics and Its Applications; Springer: Berlin/Heidelberg, Germany, 2021; Volume 126, pp. 67–127.
8. Wang, Y.; Han, H.; Liang, Z.; Yang, H.; Li, F.; Zhang, W.; Zhao, Y. Analysis of the Effect of Structural Parameters on the Internal Flow Field of Composite Curved Inlet Body Hydrocyclone. *Processes* **2024**, *12*, 2654. [CrossRef]
9. Li, F.; Liu, P.; Yang, X.; Zhang, Y. Numerical simulation on the effects of different inlet pipe structures on the flow field and separation performance in a hydrocyclone. *Powder Technol.* **2020**, *373*, 254–266. [CrossRef]
10. Dianyu, E.; Xu, G.; Fan, H.; Cui, J.; Tan, C.; Zhang, Y.; Zou, R.; Kuang, S.; Yu, A. Numerical investigation of hydrocyclone inlet configurations for improving separation performance. *Powder Technol.* **2024**, *434*, 119384. [CrossRef]
11. Wang, B.; Yu, A.B. Numerical study of particle–fluid flow in hydrocyclones with different body dimensions. *Miner. Eng.* **2006**, *19*, 1022–1033. [CrossRef]
12. Cullivan, J.C.; Williams, R.A.; Cross, R. Understanding the Hydrocyclone Separator Through Computational Fluid Dynamics. *Chem. Eng. Res. Des.* **2003**, *81*, 455–466. [CrossRef]
13. Durango-Cogollo, M.; Garcia-Bravo, J.; Newell, B.; Gonzalez-Mancera, A. CFD Modeling of Hydrocyclones—A Study of Efficiency of Hydrodynamic Reservoirs. *Fluids* **2020**, *5*, 118. [CrossRef]
14. Vieira, L.G.M.; Barrozo, M.A.S. Effect of vortex finder diameter on the performance of a novel hydrocyclone separator. *Miner. Eng.* **2014**, *57*, 50–56. [CrossRef]
15. Zhang, T.; Li, J.; Yang, D.; Wang, Z.; Zhao, W.; Fu, P.; Wang, H. High-efficiency microplastic removal in water treatment based on short flow control of hydrocyclone: Mechanism and performance. *Water Res.* **2024**, *267*, 122492. [CrossRef]
16. Fang, X.; Wang, G.; Zhong, L.; Wang, D.; Qiu, S.; Li, X. Analysis of weakly cemented gas hydrate bearing sediments particles movement and de-cementation behavior in hydrocyclone separator. *Powder Technol.* **2023**, *424*, 118174. [CrossRef]
17. Guo, D.; Jiang, X.; Guo, M.; Zeng, M.; Wu, N.; Hao, L.; Wang, C. Role of hydrocyclone separator on the formation and separation of aerobic granular sludge: Evaluating granulation efficiency and simulating hydrodynamic behavior. *Sep. Purif. Technol.* **2022**, *283*, 120231. [CrossRef]
18. Xu, Y.; Song, X.; Sun, Z.; Tang, B.; Li, P.; Yu, J. Numerical Investigation of the Effect of the Ratio of the Vortex-Finder Diameter to the Spigot Diameter on the Steady State of the Air Core in a Hydrocyclone. *Ind. Eng. Chem. Res.* **2013**, *52*, 5470–5478. [CrossRef]
19. Zhang, Y.; Xu, M.; Hu, W.; Xu, X.; Zhang, Q. Vortex finder diameter and depth effects on the separation performance of hydrocyclone. *Chem. Eng. Res. Des.* **2023**, *195*, 181–191. [CrossRef]
20. Liu, P.; Chen, B.; Hou, D.; Jiang, Z.; Yan, Z.; Han, Z. Study on the Separation Performance of a Two Cylindrical Section Hydrocyclone under Various Height Ratios. *ACS Omega* **2024**, *9*, 21569–21579. [CrossRef] [PubMed]
21. Dabir, B. Mean Velocity Measurements in a 300 Hydrocyclone Using Laser Doppler Anemometry. Ph.D. Thesis, Chemical Engineering Department, Michigan State University, East Lansing, MI, USA, 1983.
22. Versteeg, H.K.; Malalasekera, W. *An Introduction to Computational Fluid Dynamics: The Finite Volume Method*, 2nd ed.; Pearson Education: Harlow, UK, 2007.
23. Shih, T.H.; Liou, W.W.; Shabbir, A.; Yang, Z.; Zhu, J. A new k-ε eddy viscosity model for high reynolds number turbulent flows. *Comput. Fluids* **1995**, *24*, 227–238. [CrossRef]
24. Morsi, S.A.; Alexander, A.J. An investigation of particle trajectories in two-phase flow systems. *J. Fluid Mech.* **1972**, *55*, 193–208. [CrossRef]
25. Hsieh, K.T.; Rajamani, R.K. Mathematical model of the hydrocyclone based on physics of fluid flow. *ALCHE J.* **1991**, *37*, 735–746. [CrossRef]
26. Wu, Z.; Liang, Z.; Li, P.; Li, F.; Yang, H. Effect of Vortex Finder Wall Thickness on Internal Flow Field and Classification Performance in a Hydrocyclone. *Separations* **2025**, *12*, 149. [CrossRef]
27. Fu, S.; Qian, Y.; Yuan, H.; Fang, Y. Effect of cone angles of a hydrocyclone for the separation of waste plastics with low value of density difference. *Waste Manag.* **2022**, *140*, 183–192. [CrossRef]

28. Wang, C.; Ma, Y.; Sui, W. The Secondary Flows in a Cyclone Separator: A Review. *Processes* **2023**, *11*, 2935. [CrossRef]
29. Cavalcante, D.C.M.; Magalhães, H.L.F.; Neto, S.R.F.; Gomez, R.S.; Delgado, J.M.P.Q.; Lima, A.G.B.; Vasconcelos, D.B.T.; Silva, M.J.V.; Farias, D.O.; Queiroz, S.F.A.M.; et al. Hydrodynamic Evaluation of a Filtering Hydrocyclone for Solid Particle/Water Separation. *Membranes* **2024**, *14*, 171. [CrossRef]

Disclaimer/Publisher's Note: The statements, opinions and data contained in all publications are solely those of the individual author(s) and contributor(s) and not of MDPI and/or the editor(s). MDPI and/or the editor(s) disclaim responsibility for any injury to people or property resulting from any ideas, methods, instructions or products referred to in the content.